Isolated-attosecond-pulse high-order harmonic generation of keV x rays

Hsu-hsin Chu [1,2,*] and Jyhpyng Wang [1,2,3]

[1]*Department of Physics, National Central University, Zhongli 320317, Taiwan*

[2]*Center for High Energy and High Field Physics, National Central University, Zhongli 320317, Taiwan*

[3]*Institute of Atomic and Molecular Sciences, Academia Sinica, P.O. Box 23-166, Taipei, Taiwan*

(Received 14 September 2023; accepted 19 April 2024; published 8 May 2024)

Using rare-gas ions as the interacting medium, phase-matched high-order harmonic generation up to 1-keV hard x ray can be achieved by balancing the negative plasma dispersion and Gouy phase shift with the positive, intensity-dependent, intrinsic dipole phase variation. The time-dependent phase-matching condition automatically gates the harmonic output to an isolated attosecond pulse. The estimated pulse duration is as short as 120 as.

DOI: 10.1103/PhysRevA.109.053511

I. INTRODUCTION

Over the past two decades, high-order harmonic generation (HHG) driven by intense laser pulses has proven to be a reliable coherent light source, producing ultrashort extreme-ultraviolet (EUV) and soft x-ray radiation [1–3]. Theories and experiments have established that the maximum photon energy is limited by $E_{\text{cutoff}} = I_p + 3.17U_p$, where I_p is the ionization potential of the interacting medium and U_p is the ponderomotive potential of the driving pulse [4–6]. To push the HHG output to shorter wavelengths, it is necessary to increase either I_p or U_p. Previous studies have demonstrated the generation of keV harmonic output by utilizing helium atoms as the interacting medium and employing midinfrared (MIR) as the driving source [7], since U_p scales with the driving wavelength as λ_d^2. However, the overall conversion efficiency is traded off severely due to the small single-atom response, which scales as λ_d^{-6} [8,9]. To resolve this dilemma, ion-based HHG has been demonstrated to generate shorter wavelengths than that from neutral media [10–12]. Since the bound electrons in ions have higher I_p, which can only be ionized at a higher laser intensity, U_p is also raised. Both factors lead to a higher cutoff photon energy. However, in a highly ionized medium, the severe phase-mismatch problem caused by the plasma dispersion limits the conversion efficiency [13]. These tradeoffs make generating high harmonics efficiently at short wavelengths an immense challenge. To surmount the problem of phase mismatch, quasi-phase-matching (QPM) is a possible solution [14–18]. Recently, we have proposed a QPM scheme of near-infrared (NIR)-driven keV HHG from He^{1+} ions [19], in which a transverse pulse is used to suppress the generation process from out-of-phase locations [20]. It can selectively enhance narrow-band harmonic generation within a wide spectral range, making it a promising x-ray source with high spectral brightness.

In this paper, we show that phase-matched HHG up to 1-keV photon energy can be achieved in ionic media by using an ultrashort NIR (810 nm) pulse focused onto a uniform He gas cell with optimized gas density and proper beam divergence. By setting the appropriate driving pulse focal spot size and the gas cell location relative to the focal point, phase matching is accomplished through the balance of plasma dispersion, Gouy phase shift, and the HHG intrinsic dipole phase variation, where the latter is intensity dependent and thus determined by the driving pulse divergence. Our analysis shows that under the optimized condition, the NIR driving pulse will ionize the He atoms into 1+ ions at its front edge, and then generate high-energy HHG from these ions at its peak. Since the HHG dipole phase is determined by the driving laser intensity, it varies across the driving pulse envelope. Only the harmonic wavefront initiated within a small interval around the driving pulse peak fulfills the phase-matching criteria that the accumulated total phase mismatch falls within $\pm\pi$. With an 8-fs-duration driving pulse, such a temporal gate is shorter than half of the driving laser period, enabling this scheme to generate an isolated attosecond pulse. The phase-matching bandwidth covers about five harmonic orders, supporting a pulse duration as short as 120 as. Reference [21] provides a comprehensive review of extreme-UV isolated-attosecond-pulse generation. Our scheme can push the output to keV hard x rays. It is different from the nonadiabatic self-phase matching, which relies on the rapid change of plasma density produced by a few-cycle driving pulse [22,23]. It is also different from the dynamic phase matching introduced by Thomann *et al.* [24], where isolated attosecond extreme-UV pulses were produced from multicycle NIR driving pulses. In their analysis, the HHG dipole phase was not considered, which is the key element of our scheme.

To illuminate the physics behind this scheme, we first calculate the propagation of the driving pulse in a uniform gas cell, with all the ionization, attenuation, diffraction, and dispersion effects taken into account. The driving pulse is modeled as a three-dimensional (3D) Gaussian pulse focused at position $z = 0$, and the He gas cell is put behind the focal

*hhchu@ncu.edu.tw

point. The exhaustive calculation is presented in Sec. II. The calculation provides the complete information of the driving pulse waveform, He atom and ion densities, and electron density as functions of position (z, r) and time t. After that, we can evaluate the phase-matching condition, and calculate the generation process of the specific harmonic wave. The details are presented in Secs. III and IV, respectively. Then the temporal gating effect is analyzed in Sec. V, and the robustness of this scheme is discussed in Sec. VI. Finally, the conclusion is given in Sec. VII.

II. DRIVING PULSE PROPAGATION THROUGH THE HELIUM GAS CELL

The driving pulse is modeled as a 3D Gaussian pulse focused at $z = 0$ mm. The complete waveform is

$$E_d(z,r,t) = \frac{E_0}{2}\left[\left(\frac{-ib_0}{q(z)}\right)\exp\left(\frac{ik_d r^2}{2q(z)}\right) \times \exp\left(\frac{-(t-(z-z_{\rm ini})/c)^2}{2\tau_0^2}\right) e^{i(k_d z-\omega_d t)} + \text{c.c.}\right], \tag{1}$$

where

$$E_0 = \sqrt{\frac{4\mu_0 c U_{\rm pulse}}{\pi^{3/2}\tau_0 w_0^2}} \tag{2}$$

is the peak electric field at the focal spot, $U_{\rm pulse}$ is the driving pulse energy, τ_0 is the initial pulse duration, w_0 is the focal spot waist radius, $q(z) = z - ib_0$ is the q parameter of the Gaussian beam, $b_0 = \pi w_0^2/\lambda_d = \omega_d w_0^2/(2c)$ is the confocal parameter, λ_d is the driving pulse central wavelength, $k_d = 2\pi/\lambda_d$ is its wave number in vacuum, $\omega_d = ck_d$ is the central angular frequency, and c.c. represents complex conjugate. The He gas is put between $z_{\rm ini}$ and $z_{\rm final}$ with a uniform density distribution $N_{\rm gas}$. To resolve the propagation of the driving pulse in detail, we divide the gas cell into small sections with a thickness of Δz. Each section is labeled by its position $z_j = z_{\rm ini} + (j-1)\Delta z$, where $j = 1, 2, 3, \ldots$ is the label index. Then the propagation of the driving pulse passing through each section is calculated one by one.

The driving pulse arrives the first section ($j = 1$) of the helium gas cell with a beam radius of

$$w(z_1) = w(z_{\rm ini}) = w_0\sqrt{1 + \frac{z_{\rm ini}^2}{b_0^2}}. \tag{3}$$

We calculate the ionization process at radius $r = 0$, $w(z_{\rm ini})/2$, and $w(z_{\rm ini})$, by using the Ammosov-Delone-Krainov (ADK) theory for optical-field ionization [25]. The calculation is performed within a temporal window of $[-100\,\text{fs}, +100\,\text{fs}]$. After that, the He atom density $N_{\rm He}(z_{\rm ini}, r, t)$, He^{1+} ion density $N_{\rm He1+}(z_{\rm ini}, r, t)$, He^{2+} ion density $N_{\rm He2+}(z_{\rm ini}, r, t)$, and the electron density $N_e(z_{\rm ini}, r, t)$ can be obtained.

Consider the first example of keV harmonic generation driven by a 30-fs pulse. Here we focus on He^{1+} ions as the interacting medium. The ionization potential is 54.4 eV. Under the appearance intensity of 8.7×10^{15} W/cm^2 where the He^{1+} ions can be ionized into He^{2+} ions [26], the cutoff photon energy reaches 1.7 keV driven by an 810-nm NIR pulse. Here the 655th-order harmonic (1.0-keV photon energy) is chosen for detailed analysis. The driving pulse wavelength and duration are fixed at $\lambda_d = 810$ nm and $\tau_0 = 30$ fs, respectively, which are typical values for a standard Ti:sapphire laser system. The pulse energy $U_{\rm pulse}$ is chosen to be 42 mJ. It is focused at $z = 0$ mm with a waist radius of $w_0 = 40$ μm. The helium gas cell is put between $z_{\rm ini} = 9.5$ mm and $z_{\rm final} = 11.5$ mm, with a uniform density distribution of $N_{\rm gas} = 1.35\times10^{17}$ cm^{-3}. These parameters are optimized for maximizing the 655th harmonic output. The width of the 200-fs temporal window for calculation is 6.67 times the driving pulse duration, simulating the complete ionization process. With these parameters, the calculation results of the ionization in the first gas section are shown in Fig. 1. It can be seen that all He atoms are ionized to He^{1+} ions, and about 86% He^{1+} ions are ionized to He^{2+} ions at $r = 0$, revealing that keV HHG can be generated near the central portion of the driving pulse. The final electron density reaches $N_e[z_{\rm ini}, r = 0, t_{\rm final}(z_{\rm ini})] = 2.50\times10^{17}$ cm^{-3} at the center of the driving pulse ($r = 0$), where

$$t_{\rm final}(z) = \frac{z - z_{\rm ini}}{c} + 100\ \text{fs} \tag{4}$$

is the ending time of our calculation when the driving pulse has completely passed through z.

The propagation of the driving pulse is affected by the produced plasma. However, due to the time-dependent ionization process, the front part of the driving pulse encounters lower electron density and the rear part encounters higher electron density. Therefore, we use the time-averaged electron density to simulate the propagation and dispersion effects on the driving pulse:

$$\bar{N}_e(z,r) = \frac{\int N_e(z,r,t) I_d(z,r,t)\,dt}{\int I_d(z,r,t)\,dt}, \tag{5}$$

which is weighted by the driving pulse intensity $I_d(z, r, t)$. Furthermore, the time-averaged electron density and the final He^{2+} ion density are also varied in the transverse direction. They are fitted with Gaussian curves. The results are shown in Fig. 2.

Since the transverse electron density distribution is not uniform, it leads to a wavefront distortion of the driving pulse:

$$\Delta\Phi_d(z_{\rm ini}, r) = k_d[n_{\rm plasma}(\omega_d, z_{\rm ini}, r) - 1]\Delta z, \tag{6}$$

where

$$n_{\rm plasma}(\omega, z, r) = \sqrt{1 - \frac{q_e^2 \bar{N}_e(z,r)}{\epsilon_0 m_e \omega^2}} \tag{7}$$

is the refractive index of the produced plasma for the EM wave with angular frequency ω. Due to the higher electron density at the center, the ionizing medium acts like a concave lens. This is the well-known ionization defocusing effect. The wavefront distortion $\Delta\Phi_d(z_{\rm ini}, r)$ is fitted by a parabola

$$y(r) = \frac{k_d}{2f_{\rm eff}(z_{\rm ini})} r^2 \tag{8}$$

to get the effective focal length $f_{\rm eff}(z_{\rm ini})$. Then the q parameter of the driving pulse on the next gas section, $q(z_{j+1})$, can be evaluated by incorporating the contributions of the free

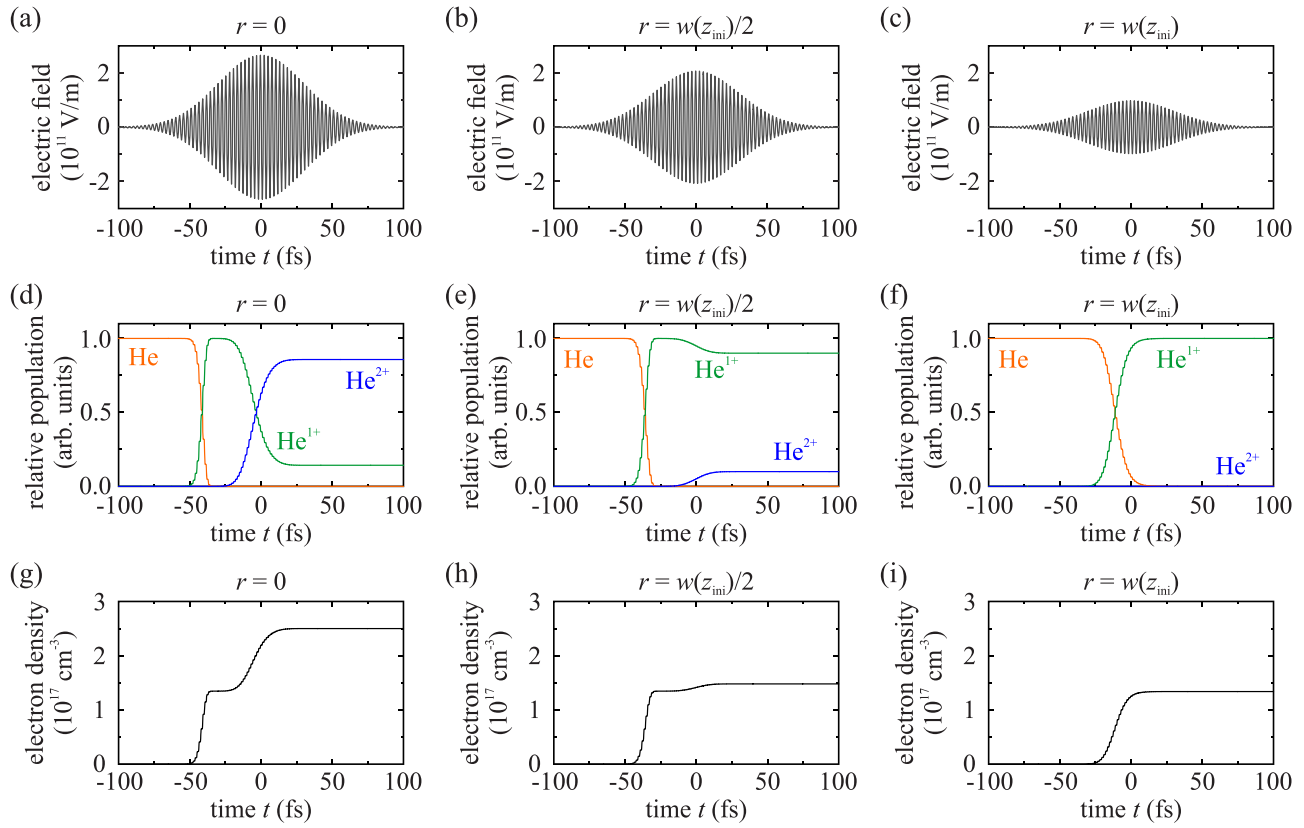

FIG. 1. Ionization of the helium gas at the first section of the gas cell ($z = z_{\rm ini}$): (a)–(c) Driving laser field $E_d(z_{\rm ini}, r, t)$ at $r = 0$, $w(z_{\rm ini})/2$, and $w(z_{\rm ini})$, respectively. (d)–(f) Relative populations of He ($N_{\rm He}/N_{\rm gas}$, orange), He^{1+} ($N_{\rm He1+}/N_{\rm gas}$, green), and He^{2+} ($N_{\rm He2+}/N_{\rm gas}$, blue) at $r = 0$, $w(z_{\rm ini})/2$, and $w(z_{\rm ini})$, respectively. (g)–(i) Electron density $N_e(z_{\rm ini}, r, t)$ at $r = 0$, $w(z_{\rm ini})/2$, and $w(z_{\rm ini})$, respectively.

propagation Δz and the effective thin lens $f_{\rm eff}(z_j)$:

$$q(z_{j+1}) = \frac{A_j q(z_j) + B_j}{C_j q(z_j) + D_j} = z'(z_{j+1}) - ib(z_{j+1}), \tag{9}$$

where

$$\begin{bmatrix} A_j & B_j \\ C_j & D_j \end{bmatrix} = \begin{bmatrix} 1 & 0 \\ -1/f_{\rm eff}(z_j) & 1 \end{bmatrix} \times \begin{bmatrix} 1 & \Delta z/n_{\rm plasma}(\omega_d, z_j, r=0) \\ 0 & 1 \end{bmatrix} \tag{10}$$

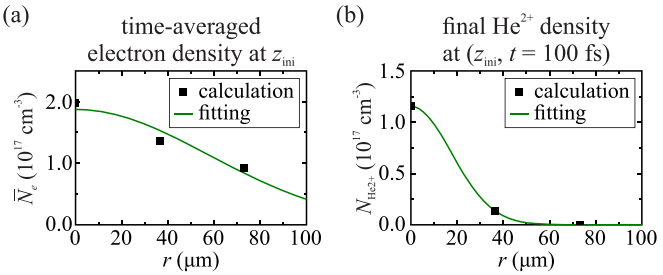

FIG. 2. (a) Time-averaged transverse electron density distribution $\bar{N}_e(z_{\rm ini}, r)$ as a function of radius r. (b) Final transverse He^{2+} density distribution $N_{\rm He2+}(z_{\rm ini}, r, t = 100\ {\rm fs})$ as a function of radius r. Black square: calculated results at $r = 0$, $w(z_{\rm ini})/2$, and $w(z_{\rm ini})$. Green line: Gaussian fitting curves.

is the *ABCD* matrix for the Gaussian beam propagation of the jth section of the gas cell. It should be noticed that $z'(z_{j+1})$ represents the real part of the q parameter in position z_{j+1} and not the position.

After the calculation of medium ionization, the attenuation of the driving pulse energy in a gas section Δz is evaluated. The following attenuation effects are taken into account:

(1) Optical-field ionization for overcoming the ionization potential: The energy loss due to overcoming the ionization potential is

$$\Delta U_{\rm ionization}(z) = \pi \left(\frac{w(z)}{2}\right)^2 \Delta z \{N_{\rm gas} I_{p1} + N_{\rm He2+}[z, r=0, t_{\rm final}(z)] I_{p2}\}, \tag{11}$$

where I_{p1} is the ionization potential of helium's first electron, and I_{p2} is the ionization potential of the second electron.

(2) Above-threshold-ionization (ATI) heating of free electron: Once an electron is ionized, it will get a kinetic energy due to the ATI-heating mechanism [25,27]:

$$K_{\rm ATI}(z, r, t_i) = \frac{q_e^2 I_d(z, r, t_i)}{c\epsilon_0 m_e \omega_d^2} \sin^2(\omega_d t_i), \tag{12}$$

where $I_d(z, r, t_i)$ is the driving laser intensity at the ionization time t_i. Therefore, the ATI heating for all free electrons leads to a driving pulse energy loss:

$$\Delta U_{\rm ATI}(z) = \sum_{\rm all\ electrons} K_{\rm ATI}(z, r, t_i). \tag{13}$$

Furthermore, for the following calculation of inverse-Bremsstrahlung heating, the electron temperature is required. It is inferred from

$$T_e(z) = \frac{2}{3}\frac{\bar{K}_{\mathrm{ATI}}(z)}{k_B}, \tag{14}$$

where $\bar{K}_{\mathrm{ATI}}(z)$ is the average kinetic energy of electron.

(3) Inverse-Bremsstrahlung heating of free electron: The absorption coefficient due to inverse-Bremsstrahlung heating is

$$a_{\mathrm{IB}}(z) = \frac{1}{3c\omega_d^2 n_{\mathrm{plasma}}(\omega_d, z, r=0)} \times \frac{q_e^6 Z(z)\bar{N}_e(z, r=0)^2 \ln[\Lambda(z)]}{2\pi\epsilon_0^2 m_e k_B T_e(z)^{3/2}}, \tag{15}$$

where $\ln[\Lambda(z)]$ is the Coulomb logarithm determined by $T_e(z)$ and $\bar{N}_e(z, r=0)$ [28].

(4) Thomson scattering by free electron: The attenuation coefficient of Thomson scattering is

$$a_{\mathrm{TS}}(z) = \frac{8\pi}{3}\frac{q_e^4}{(4\pi\epsilon_0 m_e c^2)^2}\bar{N}_e(z, r=0). \tag{16}$$

After that, the following dispersion effects are calculated:

(1) Plasma dispersion: The wave number due to plasma is

$$k_{\mathrm{plasma}}(\omega, z) = \frac{\omega}{c} n_{\mathrm{plamsa}}(\omega, z, r=0) = \frac{\omega}{c}\sqrt{1 - \frac{\omega_p(z)^2}{\omega^2}}, \tag{17}$$

where

$$\omega_p(z) = \sqrt{\frac{q_e^2 \bar{N}_e(z, r=0)}{\epsilon_0 m_e}} \tag{18}$$

is the plasma frequency. The resulted group delay from z_j to z_{j+1} is

$$\Delta C_{\mathrm{plasma}}(\omega, z_j) = \frac{\partial k_{\mathrm{plasma}}(\omega, z_j)}{\partial\omega}\Delta z = \frac{\Delta z}{c\, n_{\mathrm{plasma}}(\omega, z_j)}, \tag{19}$$

and the resulted group-delay dispersion from z_j to z_{j+1} is

$$\Delta D_{\mathrm{plasma}}(\omega, z_j) = \frac{\partial^2 k_{\mathrm{plasma}}(\omega, z_j)}{\partial\omega^2}\Delta z = \frac{-\omega_p(z_j)^2}{c[\omega^2 - \omega_p(z_j)^2]^{3/2}}\Delta z. \tag{20}$$

(2) Dispersion due to Gouy phase shift: It is well known that the Gouy phase shift of a free propagating Gaussian beam is

$$\phi_{\mathrm{Gouy}}(\omega, z) = -\tan^{-1}\left(\frac{z}{b(\omega)}\right) = -\tan^{-1}\left(\frac{2cz}{w_0^2\omega}\right), \tag{21}$$

where w_0 is the $1/e^2$-intensity radius at the beam waist. In our analysis, the Gaussian mode of the driving beam in each gas section is modified by the extra effect of ionization defocusing, as shown in Eq. (9). Therefore, the Gouy phase shift of the driving beam in the jth section of the gas cell is

$$\Delta\Phi_{\mathrm{Gouy}}(\omega_d, z_j) = k_{\mathrm{Gouy}}(\omega_d, z_j)\Delta z, \tag{22}$$

where

$$k_{\mathrm{Gouy}}(\omega_d, z_j) = \left.\frac{\partial\phi_{\mathrm{Gouy}}(\omega_d, z)}{\partial z}\right|_{z=z_j} = \frac{-b(z_j)}{z'(z_j)^2 + b(z_j)^2} = \frac{-2cw_0'(z_j)^2\omega_d}{4c^2 z'(z_j)^2 + w_0'(z_j)^4\omega_d^2} \tag{23}$$

is the additional wave number due to Gouy phase shift at z_j, and

$$w_0'(z_j) \equiv \sqrt{\frac{2cb(z_j)}{\omega_d}}. \tag{24}$$

The group delay in the jth section of the gas cell is

$$\Delta C_{\mathrm{Gouy}}(z_j) = \left.\frac{\partial k_{\mathrm{Gouy}}(\omega, z)}{\partial\omega}\right|_{\omega=\omega_d, z=z_j}\Delta z = \frac{-2c\left[4c^2 w_0'(z_j)^2 z'(z_j)^2 - w_0'(z_j)^6\omega_d^2\right]}{\left[4c^2 z'(z_j)^2 + w_0'(z_j)^4\omega_d^2\right]^2}\Delta z, \tag{25}$$

and the group-delay dispersion in the jth section of the gas cell is

$$\Delta D_{\mathrm{Gouy}}(z_j) = \left.\frac{\partial^2 k_{\mathrm{Gouy}}(\omega, z)}{\partial\omega^2}\right|_{\omega=\omega_d, z=z_j}\Delta z = \frac{4c\omega_d\left[12c^2 w_0'(z_j)^6 z'(z_j)^2 - w_0'(z_j)^{10}\omega_d^2\right]}{\left[4c^2 z'(z_j)^2 + w_0'(z_j)^4\omega_d^2\right]^3}\Delta z. \tag{26}$$

With all the information we calculated, the driving laser field at the next section ($z = z_{j+1}$) is obtained:

$$E(z_{j+1}, r, t) = E_{\mathrm{peak}}(z_{j+1})\exp\left(\frac{ikr^2}{2q(z_{j+1})}\right)\exp\left(i\sum_{k=1}^{j}[k_{\mathrm{plasma}}(\omega_d, z_k) + k_{\mathrm{Gouy}}(\omega_d, z_k)]\Delta z\right) \times \exp\left(\frac{-(t - C(z_j))^2}{2\tau(z_{j+1})^2}\right)\exp\left(i\left(\frac{1}{2}\tan^{-1}\left(\frac{D(z_j)}{\tau_0^2}\right) - \frac{D(z_j)}{2\left[\tau_0^4 + D(z_j)^2\right]}[t - C(z_j)]^2 - \omega_d t\right)\right), \tag{27}$$

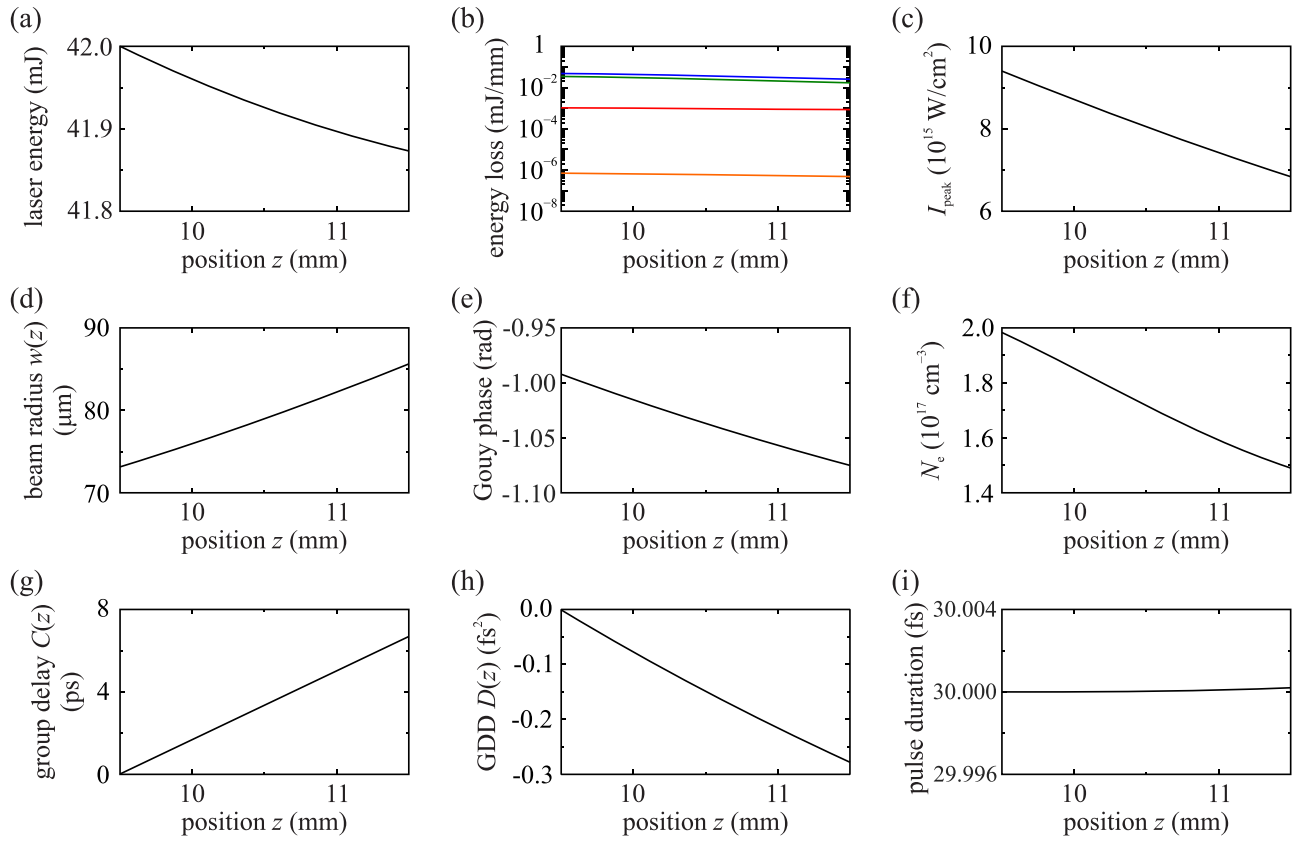

FIG. 3. (a) Driving pulse energy $U_{\text{pulse}}(z)$ as a function of position z. (b) Energy loss per unit length due to ionization loss (blue), ATI heating (green), inverse Bremsstrahlung heating (red), and Thomson scattering (orange). (c) Driving laser peak intensity $I_{\text{peak}}(z) = I[z, r = 0, t = C(z)]$. (d) Driving laser beam radius $w(z)$. (e) Gouy phase of the driving pulse. (f) Time-averaged electron density $\bar{N}_e$ at the center of the driving pulse ($r = 0$). (g) Accumulated group delay $C(z)$. (h) Accumulated group-delay dispersion (GDD) $D(z)$. (i) Driving pulse duration $\tau(z)$.

where

$$E_{\text{peak}}(z_{j+1}) = \sqrt{\frac{4\mu_0 c U_{\text{pulse}}(z_{j+1})}{\pi^{3/2}\tau(z_{j+1})w(z_{j+1})^2}} \tag{28}$$

is the peak electric field at z_{j+1}, $U_{\text{pulse}}(z_{j+1})$ is the attenuated pulse energy due to all the attenuation effects described above,

$$\tau(z_{j+1}) = \sqrt{\tau_0^2 + \frac{D(z_j)^2}{\tau_0^2}} \tag{29}$$

is the pulse duration at z_{j+1},

$$D(z_j) = \sum_{k=1}^{j} [\Delta D_{\text{plasma}}(\omega_d, z_k) + \Delta D_{\text{Gouy}}(z_k)] \tag{30}$$

is the accumulated group-delay dispersion from z_{ini} to z_{j+1}, and

$$C(z_j) = \sum_{k=1}^{j} [\Delta C_{\text{plasma}}(\omega_d, z_k) + \Delta C_{\text{Gouy}}(z_k)] \tag{31}$$

is the accumulated group delay from z_{ini} to z_{j+1}.

By iterating the processes described above, the propagation of the driving pulse passing through the helium gas cell is calculated in detail. The results are shown in Fig. 3. The energy of the driving pulse drops from 42 mJ to 41.87 mJ. The major attenuation effects are ionization loss and ATI heating loss, as shown in Fig. 3(b). The overall energy loss is insignificantly small, only about 0.3%. The peak intensity of the driving pulse drops from 9.40×10^{15} W/cm^2 to 6.84×10^{15} W/cm^2, which is mainly due to the beam divergence, as shown in Fig. 3(d). The resulted electron density is as low as about 2×10^{17} cm^{-3}, which leads to an insignificant GDD of about -0.28 fs^2. Therefore, the driving pulse duration is almost unchanged, as shown in Fig. 3(i).

The time-averaged electron density distribution $\bar{N}_e(z, r)$ and final He^{2+} density distribution $N_{\text{He2+}}[z, r, t_{\text{final}}(z)]$ are shown in Figs. 4(a) and 4(b), respectively. It can be seen that there are about 86%–28% He^{1+} ions are ionized to He^{2+} at the center of the driving pulse ($r = 0$) along the entire gas cell. Therefore, the driving pulse can continuously generate high-energy HHG photon through the He^{1+} to He^{2+} ionization and the subsequent recombination process.

To verify the correctness of our analysis, we perform a calculation for the condition of zero gas density. The beam radius variation is in perfect agreement with the analytical calculation of Gaussian beam free propagation. For the condition with 1.35×10^{17}-cm^{-3} He gas density used for 655th harmonic generation, the more divergent beam reveals the effect of plasma-induced ionization defocusing.

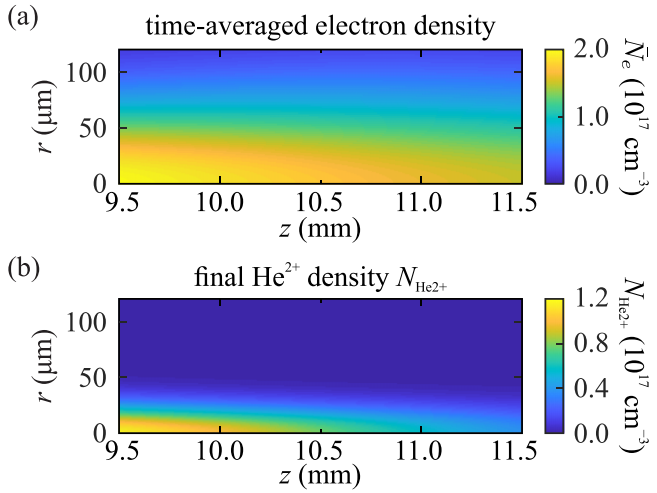

FIG. 4. (a) Time-averaged electron density $\bar{N}_e(z, r)$. (b) Final He^{2+} density $N_{He2+}[z, r, t_{final}(z)]$.

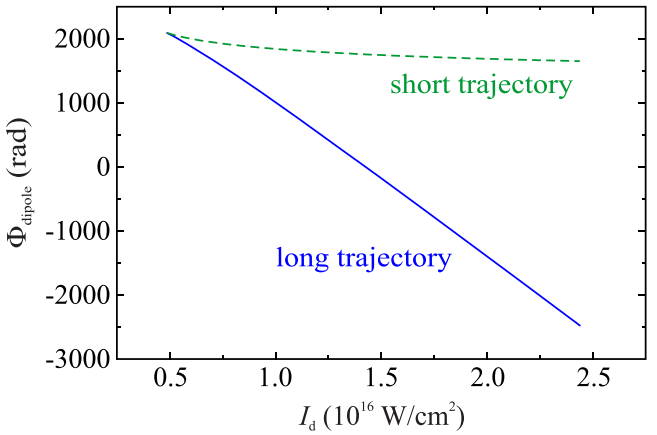

FIG. 5. The intrinsic dipole phases of the 655th harmonic as functions of the driving laser intensity I_d. Solid blue line: long-trajectory dipole phase $\Phi_{dipole,long}$. Dashed green line: short-trajectory dipole phase $\Phi_{dipole,short}$.

III. PHASE-MATCHING CONDITION OF THE 655TH HARMONIC FIELD

In this section, we analyze the phase-matching condition of the harmonic wave at the center of the driving beam ($r = 0$). Based on the quantum strong-field theory of HHG [6,29,30], it is well known that the harmonic emission exhibits an intrinsic dipole phase of

$$\Phi_{\text{dipole}} = -\frac{1}{\hbar}\int_{t_i}^{t_f}\left(\frac{[p - A(t')]^2}{2m_e} + I_p\right)dt' \tag{32}$$

for a quantum path specified by the ionization time t_i, recombination time t_f, and canonical momentum p of the electron, where $A(t')$ is the vector potential of the driving laser field. The overall dipole moment is the superposition of all possible quantum paths. For a given harmonic order m, two particular quantum paths dominate the overall dipole moment. It converges to the long-trajectory and the short-trajectory paths introduced in the semiclassical three-step model, where HHG is described by the process of electron ionization, acceleration, and then recombination driven by the laser field [5]. For the long-trajectory path, the electron is ionized earlier but recombined later. Therefore, it goes through a longer trajectory. For the short-trajectory path, the situation is exactly the opposite. These two paths give the electrons the same kinetic energy at their recombination, resulting in the same order harmonic emission. Based on the three-step model, these two dipole phases of the 655th-harmonic generation as functions of the driving laser intensity are calculated. The results are shown in Fig. 5.

Secondly, the wave number of a Gaussian beam with angular frequency ω propagating in the ionized medium is the summation of the wave number due to the produced plasma [Eq. (17)] and the additional wave number due to the Gouy phase shift [Eq. (23)]:

$$k(\omega, z) = k_{\text{plasma}}(\omega, z) + k_{\text{Gouy}}(\omega, z). \tag{33}$$

Since the phase of the harmonic field is equal to m times the phase of the driving laser field plus the intrinsic dipole phase [30], the phase-matching condition of HHG can be expressed by the wave-number mismatch

$$\begin{aligned}\Delta k(z) &= mk(\omega_d, z) - k(\omega_m, z) + \Delta k_{\text{dipole}}(z)\\ &= \Delta k_{\text{plasma}}(z) + \Delta k_{\text{Gouy}}(z) + \Delta k_{\text{dipole}}(z),\end{aligned} \tag{34}$$

where $\omega_m = m\omega_d$ is the harmonic angular frequency,

$$\Delta k_{\text{dipole}}(z) = \frac{d\Phi_{\text{dipole}}(z)}{dz} \tag{35}$$

is the wave-number mismatch due to HHG intrinsic dipole phase variation,

$$\Delta k_{\text{plasma}}(z) = mk_{\text{plasma}}(\omega_d, z) - k_{\text{plasma}}(\omega_m, z) \tag{36}$$

is the wave-number mismatch due to plasma dispersion, and

$$\Delta k_{\text{Gouy}}(z) = mk_{\text{Gouy}}(\omega_d, z) - k_{\text{Gouy}}(\omega_m, z) \tag{37}$$

is the wave-number mismatch due to Gouy phase shift. The neutral gas dispersion is neglected here since all atoms are ionized in our case. The magnitude of $\Delta k(z)$ determines whether the harmonic wave can be accumulated constructively to get efficient HHG. As mentioned in Eq. (9), the Gaussian mode of the driving pulse is modified by the effect of ionization defocusing. The driving pulse wave number due to Gouy phase shift $k_{\text{Gouy}}(\omega_d, z)$ is determined by Eq. (23). For the Gouy phase shift of the harmonic wave, the situation is the same. Its propagation is also affected by the plasma. Its q parameter is

$$q_m(z_j) = z'_m(z_j) - ib_m(z_j). \tag{38}$$

The starting confocal parameter is

$$b_m(z_{\text{ini}}) = \frac{\omega_m w_{m0}^2}{2c}, \tag{39}$$

where w_{m0} is the starting beam waist radius, which is determined by the source distribution introduced in Sec. IV. Then $q_m(z_j)$ is calculated through the similar iteration process described in the last section, and $k_{\text{Gouy}}(\omega_m, z_j)$ is

$$k_{\text{Gouy}}(\omega_m, z_j) = \frac{-b_m(z_j)}{z'_m(z_j)^2 + b_m(z_j)^2}. \tag{40}$$

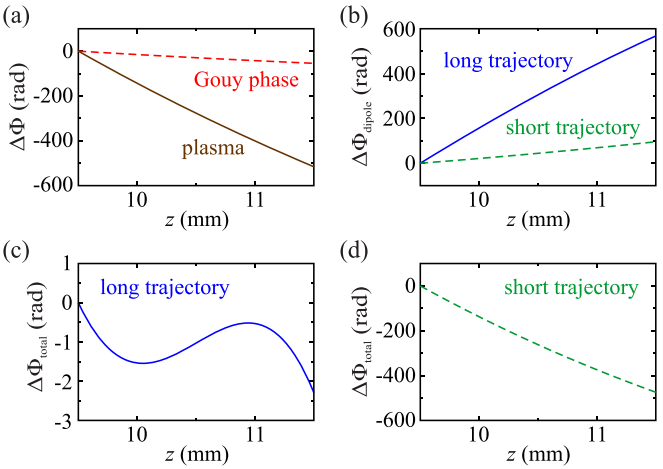

FIG. 6. (a) Accumulated phase mismatches due to plasma dispersion (solid brown line) and Gouy phase shift (dashed red line). (b) Accumulated phase mismatches due to long-trajectory dipole phase (solid blue line) and short-trajectory dipole phase (dashed green line). (c) Total phase mismatch of the 655th long-trajectory harmonic wave. (d) Total phase mismatch of the 655th short-trajectory harmonic wave.

Finally, the total accumulated phase mismatch at position z can be obtained

$$\begin{aligned}\Delta\Phi_{\text{total}}(z) &= \int_{z_{\text{ini}}}^{z} \Delta k(z')\,dz' \\ &= \Delta\Phi_{\text{plasma}}(z) + \Delta\Phi_{\text{Gouy}}(z) + \Delta\Phi_{\text{dipole}}(z),\end{aligned} \tag{41}$$

where

$$\Delta\Phi_{\text{plasma}}(z) = \int_{z_{\text{ini}}}^{z} \Delta k_{\text{plasma}}(z')\,dz' \tag{42}$$

is the accumulated phase mismatch due to plasma dispersion,

$$\Delta\Phi_{\text{Gouy}}(z) = \int_{z_{\text{ini}}}^{z} \Delta k_{\text{Gouy}}(z')\,dz' \tag{43}$$

is the accumulated phase mismatch due to Gouy phase shift,

$$\Delta\Phi_{\text{dipole}}(z) = \Phi_{\text{dipole}}(z) - \Phi_{\text{dipole}}(z_{\text{ini}}) \tag{44}$$

is the accumulated phase mismatch due to HHG dipole phase variation, $\Phi_{\text{dipole}}(z) = \Phi_{\text{dipole}}\{I_d[z, t_{\text{HWF}}(z)]\}$ is the HHG dipole phase determined by the harmonic order m and the driving pulse intensity met by the fixed harmonic wavefront at position z, and $t_{\text{HWF}}(z)$ is the arriving time of the fixed harmonic wavefront at position z, as explained in Eq. (45) in the next section. It is important to note that the harmonic wave number due to the produced plasma $k_{\text{plasma}}(\omega_m, z)$ is evaluated by applying the transient electron density $N_e[z, r = 0, t_{\text{HWF}}(z)]$ encountered by the harmonic wavefront. The calculation results of these phase mismatches are shown in Fig. 6.

It is evident that the phase mismatch caused by the plasma dispersion is negative. It reaches about −516 rad at the end of the gas cell. The phase mismatch caused by the Gouy phase shift is also negative, but the magnitude is only about 1/10 of the plasma dispersion. The phase mismatches caused by the dipole phase variations are both positive. In particular, the phase mismatch due to the long-trajectory dipole phase is large enough to compensate for the negative plasma dispersion and Gouy phase shift. Therefore, the total phase mismatch fulfills the phase-matching criteria ($|\Delta\Phi_{\text{total}} < \pi|$) along the entire gas cell, as shown in Fig. 6(c). At the same time, the total phase mismatch of the short-trajectory emission is still dominated by the plasma dispersion. It reaches about −474 rad at the end of the gas cell, as shown in Fig. 6(d). In short, phase matching is achieved for the long-trajectory harmonic emission by balancing the negative plasma dispersion, Gouy phase shift, and the positive dipole phase variation.

IV. GENERATION, PROPAGATION, AND ACCUMULATION OF THE 655TH HARMONIC FIELD

To calculate the harmonic generation process, we trace a fixed wavefront of the 655th harmonic, which is initiated at the entrance of the gas cell ($z = z_{\text{ini}}$) and on the peak of the driving pulse ($t = 0$). The wavefront propagates with a phase velocity of $v_p(\omega_m, z) = \omega_m/k(\omega_m, z)$. It arrives position z at time

$$t_{\text{HWF}}(z) = \int_{z_{\text{ini}}}^{z} \frac{1}{v_p(\omega_m, z')}\,dz'. \tag{45}$$

Since the phase velocity of the harmonic field is greater than the group velocity of the driving laser pulse, the relative location of the harmonic wavefront to the driving pulse envelope changes during the propagation. The harmonic wavefront will encounter the driving laser field

$$E_{\text{HWF}}(z) \equiv E_d[z, r = 0, t_{\text{HWF}}(z)] \tag{46}$$

when it propagates to position z. The latter will generate a new harmonic wavelet, which is coherently added to the existing harmonic field, and the HHG dipole phase at z is evaluated from the intensity of the driving pulse at z, as mentioned in the last paragraph.

According to the empirical semiclassical model proposed in Ref. [31] and verified in Refs. [16,20], the locally generated infinitesimal harmonic wavelet $E_{\text{LH}}(z)$ at position z can be simulated as

$$E_{\text{LH}}(z) \propto N_{\text{source}}(z)\,|E_{\text{HWF}}(z)|^p\,e^{i\Phi_{\text{LH}}(z)}, \tag{47}$$

where its amplitude is proportional to the source density $N_{\text{source}}(z)$ times the pth power of the driving field amplitude $|E_{\text{HWF}}(z)|$. The number p is an empirical constant between 5–7 [31]. The result of our analysis is not sensitive to the choice of $p(= 5)$ in this range. Because the harmonic is generated from the $He^{1+} \rightarrow He^{2+}$ ionization and the following recombination process, where the recombination probability is fixed for a specified harmonic order, the source density is

$$N_{\text{source}}(z) \propto N_{\text{He1+}}[z, r = 0, t_{\text{HWF}}(z)]\,w_{\text{He1+}}[E_{\text{HWF}}(z)], \tag{48}$$

where $N_{\text{He1+}}[z, r = 0, t_{\text{HWF}}(z)]$ is the remaining He^{1+} density met by the fixed harmonic wavefront at position z, and $w_{\text{He1+}}[E_{\text{HWF}}(z)]$ is the ionization rate of He^{1+} ions at z [25]. The phase of the locally generated infinitesimal harmonic wavelet $\Phi_{\text{LH}}(z)$ is

$$\Phi_{\text{LH}}(z) = m\Phi_{\text{HWF}}(z) + \Phi_{\text{dipole}}(z), \tag{49}$$

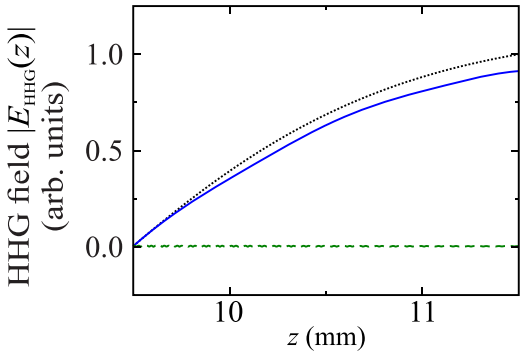

FIG. 7. The amplitude of the accumulated 655th-order harmonic field. Dotted black line: perfect phase-matching condition, solid blue line: long-trajectory harmonic wave, dashed green line: short-trajectory harmonic wave.

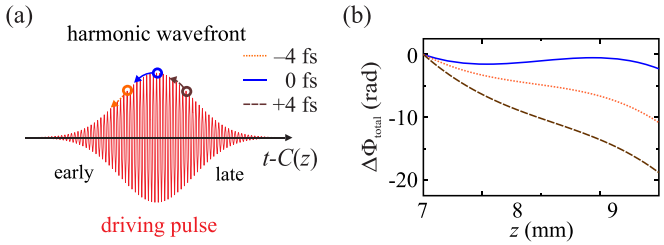

FIG. 8. (a) The schematic diagram of the locations of the harmonic wavefronts initiated at $t_0 = -4$ fs (dotted orange line), 0 fs (solid blue line), and +4 fs (dashed brown line) relative to the driving laser field (red line). The arrows indicate the change of harmonic wavefront locations due to propagation. (b) The total accumulated phase mismatches $\Delta\Phi_{\text{total}}(z)$ for these three harmonic wavefronts.

where $\Phi_{\text{HWF}}(z) = \arg[E_{\text{HWF}}(z)]$ is the phase of the driving laser field, and $\Phi_{\text{dipole}}(z) = \Phi_{\text{dipole}}\{I_d[z, r = 0, t_{\text{HWF}}(z)]\}$ is the intrinsic dipole phase.

Since the driving beam diverges during its propagation, the intensity decreases. Therefore, the ionization rate $w_{\text{He1+}}$ decreases, and the remaining He^{1+} density increases. Then the source density reaches its maximum around the middle part of the gas cell. Such condition benefits the HHG output.

As a result of a fixed harmonic wavefront being traced, the accumulated harmonic field $E_{\text{HHG}}(z)$ as a function of position z can be obtained by integrating the locally generated infinitesimal harmonic wavelet:

$$E_{\text{HHG}}(z) \propto \int_{z_{\text{ini}}}^{z} E_{\text{LH}}(z')\, dz'. \tag{50}$$

The results are shown in Fig. 7. For the 655th long-trajectory harmonic generation, the final field strength reaches 92% of the ideal magnitude under perfect phase matching. The relative energy conversion efficiency is 85%. In contrast, the severe phase mismatch of the short-trajectory emission inhibits its growth. Its accumulated field remains low.

V. TEMPORAL-GATING EFFECT OF THE 655TH HARMONIC FIELD

Continue the case of the 655th long-trajectory harmonic driven by an 810-nm, 30-fs laser pulse. Since the phase velocity of the harmonic field is greater than the group velocity of the driving pulse, harmonic wavefronts initiated at different starting times t_0 slip over different portions of the driving pulse envelope. The locations of the harmonic wavefronts initiated at starting time $t_0 = -4$, 0, and +4 fs relative to the driving pulse peak are shown in Fig. 8(a). The driving laser intensities met by these three harmonic wavefronts are different during the driving pulse propagation. Therefore, the resulting dipole phases are also different. Furthermore, since the electron densities encountered by these harmonic wavefronts are also varied, the phase mismatches due to plasma dispersion are different, too. These two effects lead to different total phase mismatches, as shown in Fig. 8(b). It is clear that the harmonic wavefronts initiated at $t_0 = \pm 4$ fs accumulate phase mismatches far beyond $\pm\pi$, revealing that there only exists a small temporal window around the peak of the driving pulse, which fulfills the phase-matching criteria.

To evaluate the effect of such temporal gating, we calculate the accumulated harmonic field $E_{\text{HHG}}(z, t_0)$ initiated at different t_0. The final intensity $I_{\text{HHG}}(t_0) \propto |E_{\text{HHG}}(z_{\text{final}}, t_0)|^2$ is shown in Fig. 9(a). As expected, a narrow temporal window is obtained. The full-width at half-maximum (FWHM) of the window is about 4.0 fs. The phase matching bandwidth is evaluated by calculating the accumulated harmonic field with $t_0 = 0$ for different harmonic orders under the same condition. The results are shown in Fig. 9(b). It covers about three harmonic orders of $\Delta\omega = 8.4\times10^{15}$ sec^{-1} (FWHM).

The gating width can be shortened with a shorter driving pulse duration. For example, after optimization, we find that by using an 8-fs driving pulse of 23-mJ energy and 55-μm focal spot waist radius, and putting the He gas cell between $z_{\text{ini}} = 19$ mm and $z_{\text{final}} = 21$ mm with a density of 9.1×10^{16} cm^{-3}, the resulting temporal gating width is 1.2 fs, as shown in Fig. 10(a). Such width is shorter than half of the 2.7-fs driving laser period, ensuring that the generated harmonic pulse will be an isolated attosecond pulse. The phase-matching bandwidth is about 1.4×10^{16} sec^{-1} (FWHM), as shown in Fig. 10(b). With proper dispersion compensation, such bandwidth can support a transform-limited pulse with 120-as duration (FWHM).

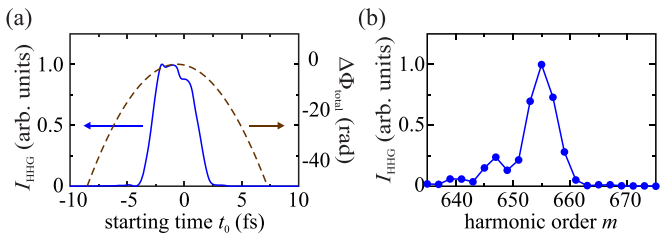

FIG. 9. Temporal gating effect of the 30-fs driving pulse. (a) The intensity of the 655th long-trajectory harmonic field I_{HHG} (solid blue line) and the accumulated total phase mismatch $\Delta\Phi_{\text{total}}$ (dashed brown line) at the end of the gas cell as functions of the starting time t_0. (b) The intensity for different harmonic orders at the end of the gas cell.

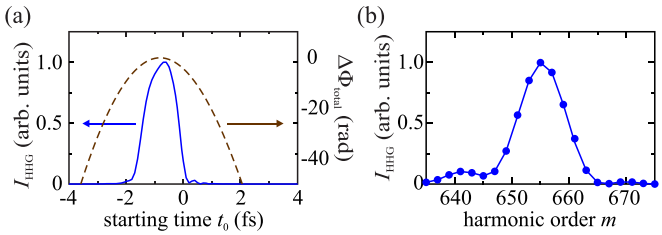

FIG. 10. Temporal gating effect of the 8-fs driving pulse. (a) The intensity of the 655th long-trajectory harmonic field I_{HHG} (solid blue line) and the accumulated total phase mismatch $\Delta\Phi_{total}$ (dashed brown line) at the end of the gas cell as functions of the starting time t_0. (b) The intensity for different harmonic orders at the end of the gas cell.

VI. DISCUSSION

Since the phase-matching condition depends on the driving laser intensity, the energy fluctuation of the driving pulse may affect the output HHG. To evaluate this effect, we repeat the calculation of the 655th long-trajectory harmonic generation driven by the 8-fs pulse with ±1% energy fluctuation, which is a typical specification of a common Ti:sapphire laser. The results are shown in Fig. 11(a). It reveals that the central timing of the temporal window is unchanged, but the height of its peak fluctuates with +4/−14%, and its width varies with +0.4/−0.1 fs. Since the width variation is much smaller than half of the driving laser period, the output HHG pulse remains an isolated attosecond pulse with negligible timing jitter and ±9% energy fluctuation.

Furthermore, the output fluctuation caused by the gas density fluctuation is also evaluated by repeating the calculation of the harmonic generation process with ±0.5% He gas density. The results are shown in Fig. 11(b). The peak fluctuates about ±5%, and the width varies −0.2/+ 0.3 fs. These analyses show that precise control of the experimental condition is necessary for a stable HHG output.

On the other hand, the self-phase modulation caused by the rapid change of the electron density due to optical-field ionization may affect the phase-matching condition. The variation of the electron density leads to the change of the plasma

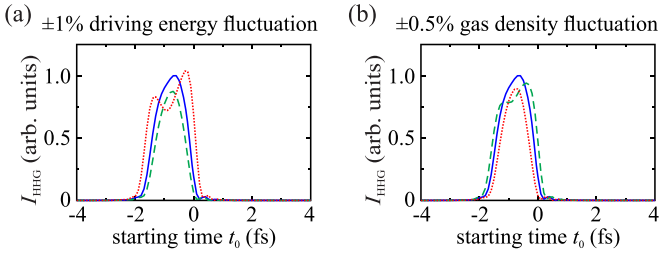

FIG. 11. (a) The intensities of the 655th long-trajectory harmonic field I_{HHG} at the end of the gas cell as functions of the starting time t_0. Solid blue line: original driving energy, dotted red line: +1% driving energy, dashed green line: −1% driving energy. (b) The intensities of the 655th long-trajectory harmonic field I_{HHG} at the end of the gas cell as functions of the starting time t_0. Solid blue line: original gas dnesity, dotted red line: +0.5% gas density, dashed green line: −0.5% gas density.

refractive index and thus the phase modulation of the driving pulse. Such modulation results in the shift of the driving laser angular frequency:

$$\Delta\omega_d = -k_d \frac{dn_{\text{plasma}}}{dt} L = \frac{k_d}{2n_{\text{plasma}} N_{\text{cr}}} \frac{dN_e}{dt} L, \qquad (51)$$

where N_{cr} is the critical density of the driving laser field and L is the interaction length. In our analysis, dN_e/dt is about 3.3×10^{15} cm^{-3} fs^{-1} and $L = 2$ mm. The resulted angular frequency shift is about 1.5×10^{13} sec^{-1}, which is only 0.6% of the driving pulse central angular frequency. It not only falls within the original bandwidth of the driving pulse, but also its HHG frequency falls within the HHG phase-matching bandwidth. The self-phase modulation may only induce an additional 0.6% phase shift of the driving pulse. It will only change the optimal plasma density slightly and will not affect the model of our calculation. Therefore, the effect of self-phase modulation is neglected in our analysis.

VII. CONCLUSION

Compared with previous demonstrations of keV HHG driven by MIR [7], our scheme uses NIR as the driving source. A 10^4-fold enhancement of the conversion efficiency is expected, due to the λ_d^{-6} dependence of the HHG single-atom response [8,9,32]. Furthermore, only a moderate gas density is required in our scheme since a large fraction of the medium participates in the interaction. In contrast, in keV HHG with MIR pulse as the pumping source, the strict phase-matching condition limits its ionization ratio of the interacting gas to only 0.03% [7]. Therefore, even though the applied gas density is as high as several tens of bars, the density of the interacting medium that actually contributes to the generation process was only similar to that of our scheme.

In short, a scheme of ion-based keV HHG is analyzed. By precisely controlling the divergence of the driving laser pulse, phase matching of the 655th-order long-trajectory harmonic generation can be achieved by balancing the plasma dispersion, Gouy phase shift, and dipole phase variation. The amplitude of the accumulated harmonic field reaches 85% relative to the ideal condition of perfect phase matching. The intensity-dependent phase-matching condition acts as a temporal gate shorter than half of the driving pulse period, ensuring that the output pulse is automatically an isolated-attosecond pulse. The phase-matching bandwidth supports a transform-limited pulse duration of about 120 as. This method can be applied over a wide HHG spectral range and for different driving wavelengths. We believe this ion-based phase-matched HHG scheme is a promising keV x-ray source for research of ultrafast phenomena.

ACKNOWLEDGMENTS

This work was supported by the National Science and Technology Council, Taiwan under Grants No. MOST 111-2221-E-001-003, No. MOST 111-2112-M-008-016, No. NTSC 112-2119-M-001-008, and No. NSTC 112-2112-M-008-013.

[1] T. Brabec and F. Krausz, Rev. Mod. Phys. **72**, 545 (2000).
[2] P. B. Corkum and F. Krausz, Nature Phys. **3**, 381 (2007).
[3] H. Kapteyn, O. Cohen, I. Christov, and M. Murnane, Science **317**, 775 (2007).
[4] A. L'Huillier, K. J. Schafer, and K. C. Kulander, J. Phys. B: At. Mol. Opt. Phys. **24**, 3315 (1991).
[5] P. B. Corkum, Phys. Rev. Lett. **71**, 1994 (1993).
[6] M. Lewenstein, P. Balcou, M. Y. Ivanov, A. L'Huillier, and P. B. Corkum, Phys. Rev. A **49**, 2117 (1994).
[7] T. Popmintchev, M.-C. Chen, D. Popmintchev, P. Arpin, S. Brown, S. Ališauskas, G. Andriukaitis, T. Balčiunas, O. D. Mücke, A. Pugzlys, A. Baltuška, B. Shim, S. E. Schrauth, A. Gaeta, C. Hernández-García, L. Plaja, A. Becker, A. Jaron-Becker, M. M. Murnane, and H. C. Kapteyn, Science **336**, 1287 (2012).
[8] J. Tate, T. Auguste, H. G. Muller, P. Salières, P. Agostini, and L. F. DiMauro, Phys. Rev. Lett. **98**, 013901 (2007).
[9] M. V. Frolov, N. L. Manakov, and A. F. Starace, Phys. Rev. Lett. **100**, 173001 (2008).
[10] E. A. Gibson, A. Paul, N. Wagner, R. Tobey, S. Backus, I. P. Christov, M. M. Murnane, and H. C. Kapteyn, Phys. Rev. Lett. **92**, 033001 (2004).
[11] M. Zepf, B. Dromey, M. Landreman, P. Foster, and S. M. Hooker, Phys. Rev. Lett. **99**, 143901 (2007).
[12] P. Arpin, T. Popmintchev, N. L. Wagner, A. L. Lytle, O. Cohen, H. C. Kapteyn, and M. M. Murnane, Phys. Rev. Lett. **103**, 143901 (2009).
[13] B. A. Reagan, T. Popmintchev, M. E. Grisham, D. M. Gaudiosi, M. Berrill, O. Cohen, B. C. Walker, M. M. Murnane, J. J. Rocca, and H. C. Kapteyn, Phys. Rev. A **76**, 013816 (2007).
[14] J. Seres, V. S. Yakovlev, E. Seres, C. Streli, P. Wobrauschek, C. Spielmann, and F. Krausz, Nat. Phys. **3**, 878 (2007).
[15] E. A. Gibson, A. Paul, N. Wagner, R. Tobey, D. Gaudiosi, S. Backus, I. P. Christov, A. Aquila, E. M. Gullikson, D. T. Attwood, M. M. Murnane, and H. C. Kapteyn, Science **302**, 95 (2003).
[16] S. L. Voronov, I. Kohl, J. B. Madsen, J. Simmons, N. Terry, J. Titensor, Q. Wang, and J. Peatross, Phys. Rev. Lett. **87**, 133902 (2001).
[17] K. O'Keeffe, D. T. Lloyd, and S. M. Hooker, Opt. Express **22**, 7722 (2014).
[18] L. Hareli, L. Lobachinsky, G. Shoulga, Y. Eliezer, L. Michaeli, and A. Bahabad, Phys. Rev. Lett. **120**, 183902 (2018).
[19] Y.-L. Liu, J. Wang, and H.-H. Chu, Opt. Express **30**, 1365 (2022).
[20] Y.-L. Liu, S.-C. Kao, Y.-Y. Ou Yang, Z.-M. Zhang, J. Wang, and H.-H. Chu, Phys. Rev. A **104**, 023112 (2021).
[21] M. B. Gaarde, J. L. Tate, and K. J. Schafer, J. Phys. B: At. Mol. Opt. Phys. **41**, 132001 (2008).
[22] G. Tempea, M. Geissler, M. Schnürer, and T. Brabec, Phys. Rev. Lett. **84**, 4329 (2000).
[23] M. Geissler, G. Tempea, and T. Brabec, Phys. Rev. A **62**, 033817 (2000).
[24] I. Thomann, A. Bahabad, X. Liu, R. Trebino, M. M. Murnane, and H. C. Kapteyn, Opt. Express **17**, 4611 (2009).
[25] M. V. Ammosov, N. B. Delone, and V. P. Krainov, J. Exp. Theor. Phys. **64**, 1191 (1986).
[26] S. Augst, D. Strickland, D. D. Meyerhofer, S. L. Chin, and J. H. Eberly, Phys. Rev. Lett. **63**, 2212 (1989).
[27] P. B. Corkum and N. H. Burnett, in *Short-Wavelength Coherent Radiations: Generation and Applications*, edited by R. W. Falcone and J. Kirz (OSA, Washington, DC, 1988), p. 225.
[28] D. Attwood, *Soft X-Rays and Extreme Ultraviolet Radiation: Principles and Applications* (Cambridge University Press, Cambridge, 1999), pp. 225–226.
[29] M. Lewenstein, K. C. Kulander, K. J. Schafer, and P. H. Bucksbaum, Phys. Rev. A **51**, 1495 (1995).
[30] P. Balcou, P. Sali'eres, A. L'Huillier, and M. Lewenstein, Phys. Rev. A **55**, 3204 (1997).
[31] J. Peatross, S. Voronov, and I. Prokopovich, Opt. Express **1**, 114 (1997).
[32] J. A. Pérez-Hernández, L. Roso, and L. Plaja, Opt. Express **17**, 9891 (2009).